IEEE Access
Multidisciplinary | Rapid Review | Open Access Journal

Received March 3, 2020, accepted March 17, 2020, date of publication March 23, 2020, date of current version March 31, 2020.

Digital Object Identifier 10.1109/ACCESS.2020.2982506

A New Cycle Slip Detection and Repair Method for Galileo Four-Frequency Observations

JIAN CHEN[1], DONGJIE YUE[1], SHAOLIN ZHU[1], ZHIQIANG LIU[1], XINGWANG ZHAO[2], AND WEI XU[3]

[1]School of Earth Science and Engineering, Hohai University, Nanjing 211100, China
[2]School of Geodesy and Geomatics, Anhui University of Science and Technology, Huainan 232001, China
[3]School of Geodesy and Geomatics, Wuhan University, Wuhan 430000, China

Correspondence author: Jian Chen (CJ_19930815@163.com)

This work was supported in part by the Postgraduate Research and Practice Innovation Program of Jiangsu Province under Grant SJKY19_0513 and Grant 2019B60114, in part by the National Natural Science Foundation of China under Grant 41604018 and Grant 41704008, in part by the Fundamental Research Funds for the Central Universities under Grant 2019B17514, and in part by the Program for Excellent Talents in University of Anhui Province of China under Grant gxyq2017008.

ABSTRACT Galileo four-frequency cycle slip detection and repair (CDR) is susceptible to the noise of pseudo-range observations. In this study, the Galileo four-frequency carrier phase smoothed pseudo-range (CPSP) assisted CDR method was proposed. Such method was conducted in three steps in sequence. First, the four linear independent combinations of the Galileo four-frequency observation were taken for CDR. Second, the non-divergent Hatch filter was employed to carry out the pseudo-range observation smoothly. Third, the true cycle slip was determined by rounding the float value using the least square method. To take the optimal combination of the CDR and verify the feasibility of the proposed method, the Galileo observations with satellites in different types were performed. According to the experimental results, (1) the four linear independent combinations of the geometry-free carrier phase combination (0, 1, 0, −1), (1, 1, −1, −1), (1, 2, −2, −1) and geometry-free and ionosphere-free combination (0, 0, 1, −1) were adopted for the cycle slip detection; (2) The success rate of cycle slip repair reached over 99.99% after four-frequency CPSP processing. With the CPSP assisted CDR method, the differences of the root mean square (RMS) between float and true values were down-regulated by 79.61%, 70.03%, 66.25% and 72.75%, respectively. (3) The differences of the root mean square (RMS) between float and true values were down-regulated by 13.62%, 10.67%, 10.67% and 10.67% after smoothing, respectively. In summary, the Galileo four-frequency CDR was effectively performed by the proposed method in active ionospheric area.

INDEX TERMS Carrier-phase smoothed pseudo-range, cycle slip detection and repair, Galileo, four-frequency, observation noise.

I. INTRODUCTION

Carrier phase observations are applied to high-precision Global Navigation Satellite System (GNSS) positioning, which covers real-time kinematic (RTK) and precise point positioning (PPP). Nevertheless, carrier phase observations are likely to be adversely affected by cycle slips that are attributed to obstructions of the satellite signal, multipath and high receiver dynamics, etc. Thus, the cycle slip detection and repair (CDR) is critical to high-precision GNSS positioning [1]–[4].

The associate editor coordinating the review of this manuscript and approving it for publication was Zheng H. Zhu.

Over the past decades, numerous CDR methods have been developed by researchers worldwide. Yuan *et al.* [5] have presented the high-order difference method, and Gao and Li [6] have put forward the polynomial fitting method. Nevertheless, these methods are not capable of detecting small cycle slips for the presence of noise. Yi *et al.* [7] detected the cycle slips using Wavelet Transform. The grey theory can be adopted based on single-frequency observations [8]. A considerable number of CDR methods comply with the dual-frequency observations. De Lacy *et al.* [9] presented that the Bayesian approach could detect and correct cycle-slips by un-differenced GNSS observations even if the slip occurs by one cycle. Li *et al.* [10] proposed a method by exploiting

double-constraint of ephemeris and smoothed pseudo-range, which applied to low sampling rate data. Blewitt [11] presented the TurboEdit method, adopting the Melbourne-Wubbena (MW) combination as well as ionospheric residual combination. The TurboEdit method has been applied extensively in considerable software (e.g., PANDA and Bernese) [12], [13], whereas it displays two disadvantages. To be specific, it exhibits low efficiency in the case of active ionospheric, while it only applies to dual-frequency observations and cannot repair cycle slip. Some scholars have optimized the TurboEdit approach. Liu *et al.* [14] detected and repaired cycle slips using optimized TurboEdit method and Chebyshev Polynomial method. To ascertain the cycle slip on both L1 and L2 frequencies, Liu [15] developed the ionospheric total electron contents rate (TECR) and MW combination. For the detection of cycle slip in case of ionospheric scintillation, Ji *et al.* [16] put forward non-geometry-free and ionosphere-free methods. Cai *et al.* [17] developed the forward and backward moving window averaging (FBMWA) method; they also integrated the second-order, time-difference phase ionospheric residual (STPIR) method to detect and repair cycle slips as subject to high ionospheric activity. Duan *et al.* [18] established the backward moving window averaging (BMWA) algorithm based on MW combination; they also integrated the TECR algorithm for the detection of the cycle slip.

The mentioned approaches are primarily for GNSS dual-frequency observations. However, as fueled by the modernization and advancement of GNSS systems, multi-frequency signals are currently available, covering the L1 (1575.420 MHz), L2 (1227.600 MHz) and L5 (1176.450 MHz) signals of the modernizing global positioning system (GPS), B1 (1561.098 MHz), B2 (1207.140 MHz) and B3 (1268.520 MHz) signals of BeiDou navigation satellite system (BDS) and E1 (1575.420 MHz), E5a (1176.450 MHz), E5b (1207.140 MHz), E5 (1191.795 MHz), as well as E6 (1278.750 MHz) of the Galileo. For the availability of multi-frequency observations, new upsurge for CDR will be aroused. In terms of the linear combinations of triple frequency carrier phase, Richert and El-Sheimy [19] introduced the concept of optimal linear combinations of carrier phase measurements; it was established that the choice of an optimal combination was determined by the baseline length, the physical error environment, as well as the requirements of the given mission. For the five-frequency Galileo PPP, Li *et al.* [20] suggested that the convergence time of quad- and five-frequency PPP Ambiguity solution (AR) was improved compared with that of triple-frequency PPP AR. The multi-frequency signals are capable of enhancing the accuracy and reliability of CDR [21]–[24]. For the detection of the cycle slip, two groups of geometry-free carrier phase combinations and the least-squares ambiguity decorrelation adjustment (Lambda) algorithm were proposed by Dai *et al.* [25] whereas some insensitive cycle slip could not be detected. To ensure that all the cycle slips can be detected, Huang *et al.* [26] employed two groups of geometry-free carrier phase combination and a pseudo-range and carrier phase combination. Yao *et al.* [27] and Zeng *et al.* [28] have presented methods of repairing cycle slips based on space searching. These methods, however, exhibit low efficiency when processing data. Numerous scholars have employed three linear independent combinations of triple-frequency pseudo-range and carrier phase combination [29]–[31]. Nevertheless, the performance of the mentioned methods might be down-regulated as subject to high ionospheric activity. Li *et al.* [32] further proposed to make up for the ionospheric biases by exploiting the predicted ionospheric biases. To eliminate the impact of ionospheric delay, Huang *et al.* [33] applied three groups of geometry-free and ionosphere-free and ionosphere-free (GIF) combination. Though GIF combinations are independent of ionospheric delay, the success rate of cycle slip detection of GIF combinations is down-regulated when there is significant pseudo-range noise. To perform the quad-frequency cycle-slip detection, Van de Vyvere and Warnant [34] developed the first quad-frequency cycle-slip detection algorithm, benefiting from better-quality positioning, especially high ionospheric activity.

All of the mentioned methods are capable of noticeably detecting the cycle slip in carrier phase observations, whereas the effects of pseudo-range noise and multipath are not considered. There have been rare studies focusing on four-frequency CDR methods. Accordingly, the Galileo four-frequency CPSP assisted CDR method was proposed in this study. First, the characteristics of the difference methods of the Galileo CDR were investigated. Second, a non-divergent Hatch filter was adopted to perform the pseudo-range observation smoothly. Third, the true cycle slip is resolved by rounding the float value using least square method. To verify the feasibility of the method, the Galileo observations with a range of types of satellites were tested, and the success rate of CDR between original observation and CPSP was compared.

In this contribution, the Galileo four-frequency CDR methods are expounded at first in Section 2. Afterwards, a methodology of carrier phase smoothed pseudo-range (CPSP) aided real-time CDR for Galileo four-frequency observation has been proposed in Section 3.The validity of the algorithm is verified by the measured data in Section 4. Finally, important conclusions accompanied by experimental results are summarized briefly in Section 5.

II. GALILEO FOUR-FREQUENCY CDR METHOD

A. PSEUDO-RANGE AND CARRIET PHASE COMBINATION

In accordance with the Galileo four-frequency combination observations theory, with the *a, b, c* and *d* assumed as the pseudo-range combination coefficients and the *i, j k* and *m* as the carrier phase combination coefficients, the integer ambiguity of the pseudo-range and carrier phase combination is defined as:

$$N_{i,j,k,m} = \varphi_{i,j,k,m} - \frac{P_{a,b,c,d}}{\lambda_{i,j,k,m}} + \frac{\eta_{i,j,k,m} + \eta_{a,b,c,d}}{\lambda_{i,j,k,m}} I_1 + \varepsilon \quad (1)$$

With

$$\varphi_{i,j,k,m} = i\varphi_1 + j\varphi_2 + k\varphi_3 + m\varphi_4 \quad (2)$$

$$P_{a,b,c,d} = aP_1 + bP_2 + cP_3 + dP_4 \quad (3)$$

$$\lambda_{i,j,k,m} = \frac{\mathrm{C}}{if_1 + jf_2 + kf_3 + mf_4} \quad (4)$$

$$\eta_{i,j,k,m} = \frac{f_1^2(i/f_1 + j/f_2 + k/f_3 + m/f_4)}{if_1 + jf_2 + kf_3 + mf_4} \quad (5)$$

$$\eta_{a,b,c,d} = a + b\frac{f_1^2}{f_2^2} + c\frac{f_1^2}{f_3^2} + d\frac{f_1^2}{f_4^2} \quad (6)$$

$$\varepsilon = i\varepsilon_{\varphi_1} + j\varepsilon_{\varphi_2} + k\varepsilon_{\varphi_3} + m\varepsilon_{\varphi_4} + (a\varepsilon_{P_1} + b\varepsilon_{P_2} + c\varepsilon_{P_3} + d\varepsilon_{P_4})/\lambda_{i,j,k,m} \quad (7)$$

where $\varphi_1, \varphi_2, \varphi_3, \varphi_4$ and P_1, P_2, P_3, P_4 denote carrier phase and pseudo-range observations on E1, E5a, E5b and E5, respectively; f_1, f_2, f_3, f_4 and $\lambda_1, \lambda_2, \lambda_3, \lambda_4$ refer to the frequency and wavelength of corresponding carrier observation, respectively; C indicates light speed; $\varepsilon_{\varphi_1}, \varepsilon_{\varphi_2}, \varepsilon_{\varphi_3}, \varepsilon_{\varphi_4}$ and $\varepsilon_{P_1}, \varepsilon_{P_2}, \varepsilon_{P_3}, \varepsilon_{P_4}$ represent the noise of carrier phase and pseudo-range observations, respectively; $N_{i,j,k,m}$ indicates the integer ambiguity of the combination observation; $\varphi_{i,j,k,m}$ and $P_{a,b,c,d}$ represent the combination observation of carrier phase and pseudo-range observation, respectively; $\lambda_{i,j,k,m}$ refers to wavelength of the carrier phase combination observation; $\eta_{i,j,k,m}$, $\eta_{a,b,c,d}$ are the ionospheric amplification factor of the $\varphi_{i,j,k,m}$, $P_{a,b,c,d}$, respectively; I_1 is ionospheric delay on the Galileo E1 signal; ε refers to the combination observation noise.

The cycle slip value is ascertained by differencing (1) between adjacent epochs

$$\Delta N_{i,j,k,m} = \Delta\varphi_{i,j,k,m} - \frac{\Delta P_{a,b,c,d}}{\lambda_{i,j,k,m}} + K_{i,j,k,m}\Delta I_1 + \Delta\varepsilon \quad (8)$$

where $K_{i,j,k,m} = (\eta_{i,j,k,m} + \eta_{a,b,c,d})/\lambda_{i,j,k,m}$; Δ represents differencing between adjacent epochs. The ΔI_1 can be ignored at the smaller ionospheric amplification factor. $\sigma_\varphi^2, \sigma_P^2$ are assumed to be the carrier phase and pseudo-range noises, respectively. The noise $\sigma_{\Delta N_{i,j,k}}$ of (8) is expressed as:

$$\sigma_{\Delta N_{i,j,k,m}} = \sqrt{2}\sqrt{\left[(i^2+j^2+k^2+m^2)\sigma_\varphi^2 + \frac{(a^2+b^2+c^2+d^2)\sigma_P^2}{\lambda_{i,j,k,m}^2}\right]} \quad (9)$$

To minimize the pseudo-range noise, $a = b = c = d = 1/4$ was set. Some optimal pseudo-range and carrier phase combinations were taken for Galileo four-frequency cycle slip detection in Table 1 (The σ_φ is 0.01 cycle and the σ_P is 0.3 m).

Table 1 suggests that the noises of all the combinations are below 0.3 cycle. $4\sigma_{\Delta N_{i,j,k}}$ can be taken as the threshold coefficient, and the smallest cycle slip of size 1 can be detected. The Galileo four-frequency pseudo-range and carrier phase combinations were employed to repair the cycle slip, as solved by four linear independent combinations.

TABLE 1. Galileo four-frequency pseudo-range and carrier phase combination.

(i, j, k, m)	$\lambda_{i,j,k,m}$	$\eta_{i,j,k,m}$	$\sigma_{\Delta N_{i,j,k,m}}$
(-3, 1, -1, 4)	29.305	-12.253	0.074
(0, -1, 0, 1)	19.537	0.011	0.023
(0, 1, 2, -3)	19.537	0.006	0.054
(0, -1, 1, 0)	9.768	0.019	0.030
(0, -1, 2, -1)	6.512	0.028	0.048
(0, -1, 3, -2)	4.884	0.036	0.068
(0, -3, 2, 1)	3.907	0.049	0.076
(0, -4, 3, 1)	2.791	0.068	0.105
(1, 2, -4, 1)	1.028	-0.361	0.217
(1, 1, -4, 2)	0.977	-0.350	0.227
(1, 2, -2, -1)	0.930	-0.344	0.232

B. GEOMETRY-FREE AND IONOSPHERE-FREE COMBINATION

The integer ambiguity of the geometry-free and ionosphere-free combination is calculated by:

$$N_{i,j,k,m} = iN_1 + jN_2 + kN_3 + mN_4 = i\varphi_1 + j\varphi_2 + k\varphi_3 + m\varphi_4 - \frac{aP_1 + bP_2 + cP_3 + dP_4}{\lambda_{i,j,k,m}} \quad (10)$$

With

$$\begin{cases} a + b + c + d = 1 \\ a + b\dfrac{f_1^2}{f_2^2} + c\dfrac{f_1^2}{f_3^2} + d\dfrac{f_1^2}{f_4^2} = -\dfrac{\lambda_{i,j,k,m}}{\lambda_1}\left(i + j\dfrac{f_1}{f_2} + k\dfrac{f_1}{f_3} + m\dfrac{f_1}{f_4}\right) \end{cases} \quad (11)$$

Differencing (11), the observation equation between two consequent epochs is written as:

$$\Delta N_{i,j,k,m} = i\Delta\varphi_1 + j\Delta\varphi_2 + k\varphi_3 + m\varphi_4 - \frac{a\Delta P_1 + b\Delta P_2 + c\Delta P_3 + d\Delta P_4}{\lambda_{i,j,k,m}} \quad (12)$$

$\sigma_\varphi^2, \sigma_P^2$ are assumed to be the carrier phase and pseudo-range noises, respectively. The noise $\sigma_{\Delta N_{i,j,k}}$ of (13) is defined as:

$$\sigma_{\Delta N_{i,j,k,m}} = \frac{\sqrt{2(i^2+j^2+k^2+m^2)\sigma_\varphi^2 + (a^2+b^2+c^2+d^2)\sigma_P^2}}{\lambda_{i,j,k,m}} \quad (13)$$

Three optimal Galileo four-frequency geometry-free and ionosphere-free combinations are selected in Table 2 (The σ_φ is 0.01 cycle and the σ_P is 0.3 m).

TABLE 2. Galileo four-frequency geometry-free and ionosphere-free combination.

(i, j, k, m)	a	b	c	d	$\lambda_{i,j,k}$	$4\sigma_{\Delta N_{i,j,k}}$
(0, 0, 1, -1)	0.0326	0.3400	0.3051	0.3223	19.537	0.093
(0, -1, 1, 0)	0.0028	0.3524	0.3127	0.3322	9.768	0.128
(0, -2, 1, 1)	-0.0072	0.3565	0.3152	0.3355	6.512	0.205
(0, -3, 2, 1)	-0.0032	0.3548	0.3142	0.3341	3.907	0.329
(1, 2, -4, 1)	0.7145	0.0465	0.1253	0.0867	1.028	1.280
(1, 0, -1, 0)	0.5888	0.1097	0.1641	0.1374	0.814	1.328
(1, 0, 0, -1)	0.5666	0.1189	0.1697	0.1448	0.7815	1.350
(1, -1, 0, 0)	0.5438	0.1284	0.1755	0.1524	0.7514	1.370

Table 2 suggests that the geometry-free and ionosphere-free combinations (0, 0, 1, −1), (0, −1, 1, 0), (0, −2, 1, 1), (0, −3, 2, 1) are capable of detecting the cycle slip of size 1 cycle when $4\sigma_{\Delta N_{i,j,k}}$ is taken as the threshold coefficient. The special cycle slips ($\Delta N_1 = \Delta N_2 = \Delta N_3 = \Delta N_4$) cannot be detected through the geometry-free and ionosphere-free combination.

C. GEOMETRY-FREE CARRIER PHASE COMBINATION

With the coefficients α β γ and δ assumed to satisfy the condition $\alpha + \beta + \gamma + \delta = 0$, the Galileo four-frequency geometry-free carrier phase combination is expressed as:

$$\begin{aligned}&\alpha\lambda_1\varphi_1 + \beta\lambda_2\varphi_2 + \gamma\lambda_3\varphi_3 + \delta\lambda_4\varphi_4\\ &\quad = -\eta_{\alpha,\beta,\gamma,\delta}I_1 + \alpha\lambda_1 N_1\\ &\qquad + \beta\lambda_2 N_2 + \gamma\lambda_3 N_3 + \delta\lambda_4 N_4 + \varepsilon_{\alpha,\beta,\gamma,\delta}\end{aligned} \tag{14}$$

with

$$\eta_{\alpha,\beta,\gamma,\delta} = \alpha\lambda_1 + \beta\lambda_2\frac{f_1}{f_2} + \gamma\lambda_3\frac{f_1}{f_3} + \delta\lambda_4\frac{f_1}{f_4} \tag{15}$$

$$\varepsilon_{\alpha,\beta,\gamma,\delta} = \alpha\lambda_1\varepsilon_{\varphi_1} + \beta\lambda_2\varepsilon_{\varphi_2} + \gamma\lambda_3\varepsilon_{\varphi_3} + \delta\lambda_4\varepsilon_{\varphi_4} \tag{16}$$

where $\eta_{\alpha,\beta,\gamma,\delta}$ represents the ionospheric amplification factor. $\varepsilon_{\alpha,\beta,\gamma,\delta}$ denotes the noise of the combination observation.

Differencing (15) between adjacent epochs, it yields:

$$\begin{aligned}&\alpha\lambda_1\Delta\varphi_1 + \beta\lambda_2\Delta\varphi_2 + \gamma\lambda_3\Delta\varphi_3 + \delta\lambda_4\Delta\varphi_4\\ &\quad = -\eta_{\alpha,\beta,\gamma,\delta}\Delta I_1 + \alpha\lambda_1\Delta N_1\\ &\qquad + \beta\lambda_2\Delta N_2 + \gamma\lambda_3\Delta N_3 + \Delta\varepsilon_{\alpha,\beta,\gamma,\delta}\end{aligned} \tag{17}$$

Assuming that the carrier phase signals have the identical standard deviation σ_φ, the standard deviation $\sigma_{\alpha,\beta,\gamma,\delta}$ of (18) is expressed as:

$$\sigma_{\alpha,\beta,\gamma,\delta} = \sqrt{2}\sqrt{(\alpha\lambda_1)^2 + (\beta\lambda_2)^2 + (\gamma\lambda_3)^2 + (\delta\lambda_4)^2}\sigma_\varphi \tag{18}$$

With the $\sigma_\varphi = 0.01$ cycle assumed, the optimal Galileo four-frequency geometry-free carrier phase combination is listed in Table 3.

Table 3 shows that the noises of all the combinations are less than 0.02 cycle, which is much smaller than 1 cycle.

TABLE 3. Galileo four-frequency geometry-free carrier phase combination.

$(\alpha, \beta, \gamma, \delta)$	$\eta_{\alpha,\beta,\gamma,\delta}$/cycle	$\sigma_{\alpha,\beta,\gamma,\delta}$	$\leq 4\sigma_{\alpha,\beta,\gamma,\delta}$
(0, 0, 1, -1)	-0.008	0.005	846
(0, 1, -1, 0)	0.017	0.005	483
(0, 1, 0, -1)	0.009	0.005	846
(0, 1, 1, -2)	0.0003	0.009	670
(1, -1, 0, 0)	-0.151	0.004	362
(1, 0, -1, 0)	-0.134	0.004	241
(1, 0, 0, -1)	-0.142	0.004	362
(1, 1, -1, -1)	-0.125	0.007	241
(1, 2, -2, -1)	-0.108	0.011	217

TABLE 4. Joint combinations for cycle slip detection and number of insensitive cycle slip.

Joint combinations	<80
(0, 0, 1, -1), (0, 1, -1, 0), (1, 2, -2, -1)	0
(0, 0, 1, -1)、(1, -1, 0, 0), (1, 2, -2, -1)	0
(0, 0, 1, -1), (1, 0, -1, 0), (1, 2, -2, -1)	0
(0, 0, 1, -1), (1, 0, 0, -1), (1,2,-2, -1)	0
(0, 0, 1, -1), (1,1,-1, -1), (1, 2, -2, -1)	0
(0, 1, 0, -1), (1, -1, 0, 0), (1, 2, -2, -1)	0
(0, 1, 0, -1), (1, 0, -1, 0), (1, 2, -2, -1)	0
(0, 1, 0, -1), (1, 0, 0, -1), (1, 2, -2, -1)	0
(0, 1, 0, -1), (1, 1, -1, -1), (1, 2, -2, -1)	0
(0, 1, 1, -2), (1, -1, 0, 0), (1, 2, -2, -1)	0
(0, 1, 1, -2), (1, 0, -1, 0), (1, 2, -2, -1)	0
(0, 1, 1, -2), (1, 0, 0, -1), (1, 2, -2, -1)	0

Therefore, the smallest cycle slip of size 1 can be detected by a respective combination given in the table 3. Table 3 and Table 1 suggest that the standard deviation of Galileo four-frequency geometry-free carrier phase combination is smaller as compared with pseudo-range and carrier phase combination. Nevertheless, all the combinations inevitably have some insensitive cycle slips. Thus, three combinations were applied to detect cycle slip to reduce the insensitive cycle slip. Any three combinations in Table 3 were selected to yield the joint combinations, as listed in Table 4.

As revealed in Table 4, all the smaller cycle slips within 80 cycle could be ascertained by the joint combinations. Since the Galileo four-frequency geometry-free carrier phase combination is capable of forming up to three linear independent combinations, the pseudo-range and carrier phase combination should be selected to build four linear independent combinations. Combinations (0, 1, 0, −1), (1, 1, −1, −1), (1, 2, −2, −1) and one geometry-free and

ionosphere-free combination (0, 0, 1, −1) were selected, and subsequently the floating value of the cycle slip is calculated by:

$$\underbrace{\begin{bmatrix} l_1 \\ l_2 \\ l_3 \\ l_4 \end{bmatrix}}_{\boldsymbol{L}} = \underbrace{\begin{bmatrix} \alpha_1\lambda_1 & \beta_1\lambda_2 & \gamma_1\lambda_3 & \delta_1\lambda_4 \\ \alpha_2\lambda_1 & \beta_2\lambda_2 & \gamma_2\lambda_3 & \delta_2\lambda_4 \\ \alpha_3\lambda_1 & \beta_3\lambda_2 & \gamma_3\lambda_3 & \delta_3\lambda_4 \\ i_1 & j_1 & k_1 & m_1 \end{bmatrix}}_{\boldsymbol{A}} \underbrace{\begin{bmatrix} \Delta N_1 \\ \Delta N_2 \\ \Delta N_3 \\ \Delta N_4 \end{bmatrix}}_{\boldsymbol{N}} \tag{19}$$

where, (20), (21) as shown at bottom of this page.

$\sigma_\varphi = 0.01$ cycle and $\sigma_P = 0.03$ m are assumed as the carrier phase and pseudo-range noises, respectively, and the observations are independent of each other. The covariance matrix $\boldsymbol{Q}_0$ is expressed as:

$$\boldsymbol{Q}_0 = diag(\sigma_{\varphi_1}^2, \sigma_{\varphi_2}^2, \sigma_{\varphi_3}^2, \sigma_{\varphi_4}^2, \sigma_{P_1}^2, \sigma_{P_2}^2, \sigma_{P_3}^2, \sigma_{P_4}^2) \tag{22}$$

$$\boldsymbol{N} = (\boldsymbol{A}^{\mathrm{T}}\boldsymbol{P}\boldsymbol{A})^{-1}\boldsymbol{A}\boldsymbol{P}\boldsymbol{L}, \boldsymbol{P} = \boldsymbol{Q}^{-1} \tag{23}$$

$\Delta N_{\alpha_1,\beta_1,\gamma_1,\delta_1}$, $\Delta N_{\alpha_2,\beta_2,\gamma_2,\delta_2}$, $\Delta N_{\alpha_3,\beta_3,\gamma_3,\delta_3}$, $\Delta N_{i_1,j_1,k_1,m_1}$ denote the differencing value of the geometry-free carrier phase combinations (0, 1, 0, −1), (1, 1, −1, −1), (1, 2, −2, −1) and one geometry-free and ionosphere-free combination (0, 0, 1, −1), respectively.

III. CPSP AIDED REAL-TIME CDR

By directly rounding the cycle slip floating values, the mentioned three approaches for Galileo four-frequency cycle slip repair were developed. Such methods have rounding error, and the success rate of the cycle slip repair requires analysis. ΔN denotes the floating value of the cycle slip and complies with the normal distribution. $\Delta\hat{N}$ refers to the rounding solution for the floating value of the cycle slip. $\Delta\breve{N}$ indicates the true value, and the probability of obtaining the true value is expressed as:

$$P(\Delta\hat{N} = \Delta\breve{N}) = P(\left|\Delta N - \Delta\hat{N}\right| \le \frac{1}{2}) = 2\Phi(\frac{1}{2\sigma_{\Delta N}}) - 1 \tag{24}$$

with, $\Phi(x) = \int_{-\infty}^{x} \frac{1}{\sqrt{2\pi}}(-\frac{1}{2}z^2)dz$.

The noise of the Galileo pseudo-range observation is assumed as 0.3 m, the noise after the phase smoothing as 0.06 m [35], and the noise of the carrier phase observation as 0.01 cycle. In accordance with the theory of Eq. (21), the success rate of cycle slip repair with the original and smoothed pseudo-range for the Galileo pseudo-range and carrier phase combination are calculated as listed in Table 5. Also, the corresponding results for the Galileo geometry-free and ionosphere-free combination is showed in Table 6.

TABLE 5. The success rate of cycle slip repair with the original and smoothed pseudo-range for the Galileo pseudo-range and carrier phase combination (%).

Combination	Original	Smoothed
(1, 2, 1, -4)	93.69	100
(1, -1, -1, 1)	93.30	100
(1, 0, 0, -1)	93.40	100
(1, -1, 0, 0)	92.27	100

TABLE 6. The success rate of cycle slip repair with the original and smoothed pseudo-range for the Galileo geometry-free and ionosphere-free combination (%).

Combination	Original	Smoothed
(1, 2, -4, 1)	88.19	100
(1, 0, -1, 0)	86.78	100
(1, 0, 0, -1)	86.16	100
(1, -1, 0, 0)	85.60	100

It can be seen from table 5 and table 6 that the success rates of Galileo pseudo-range and carrier phase combinations (1, 2, 1, −4), (1, −1, −1, 1), (1, 0, 0, −1), and (1, −1, 0, 0) reached 100% after smoothing, and the success rates of Galileo geometry-free and ionosphere-free combination (1, 2, −4, 1), (1, 0, −1, 0), (1, 0, 0, −1) and (1, −1, 0, 0) reached 100% after smoothing, revealing that the CPSP is capable of noticeably elevating the success rate of cycle slip repair.

The non-divergent Hatch filter was employed. This method could smooth the pseudo-range of the n epoch, using the first one to n epoch observation. With multi-frequency Hatch filtering, as long as no cycle slip occurs in the carrier observations or the cycle slip will be correctly repaired [36], which can be employed throughout the study. The smoothing

$$\boldsymbol{L} = \underbrace{\begin{bmatrix} \alpha_1\lambda & \beta_1\lambda_2 & \gamma_1\lambda_3 & \delta_1\lambda_4 & 0 & 0 & 0 & 0 \\ \alpha_2\lambda_1 & \beta_2\lambda_2 & \gamma_2\lambda_3 & \delta_2\lambda_4 & 0 & 0 & 0 & 0 \\ \alpha_3\lambda_1 & \beta_3\lambda_2 & \gamma_3\lambda_3 & \delta_3\lambda_4 & 0 & 0 & 0 & 0 \\ i_1 & j_1 & k_1 & m_1 & \frac{-1}{a\lambda_{i_1,j_1,k_1,m_1}} & \frac{-1}{b\lambda_{i_1,j_1,k_1,m_1}} & \frac{-1}{c\lambda_{i_1,j_1,k_1,m_1}} & \frac{-1}{d\lambda_{i_1,j_1,k_1,m_1}} \end{bmatrix}}_{\boldsymbol{B}} \begin{bmatrix} l_{\varphi_1} \\ l_{\varphi_2} \\ l_{\varphi_3} \\ l_{\varphi_4} \\ l_{P_1} \\ l_{P_2} \\ l_{P_3} \\ l_{P_4} \end{bmatrix} \tag{20}$$

$$\boldsymbol{Q} = \boldsymbol{B}\boldsymbol{Q}_0\boldsymbol{B}^{\mathrm{T}} \tag{21}$$

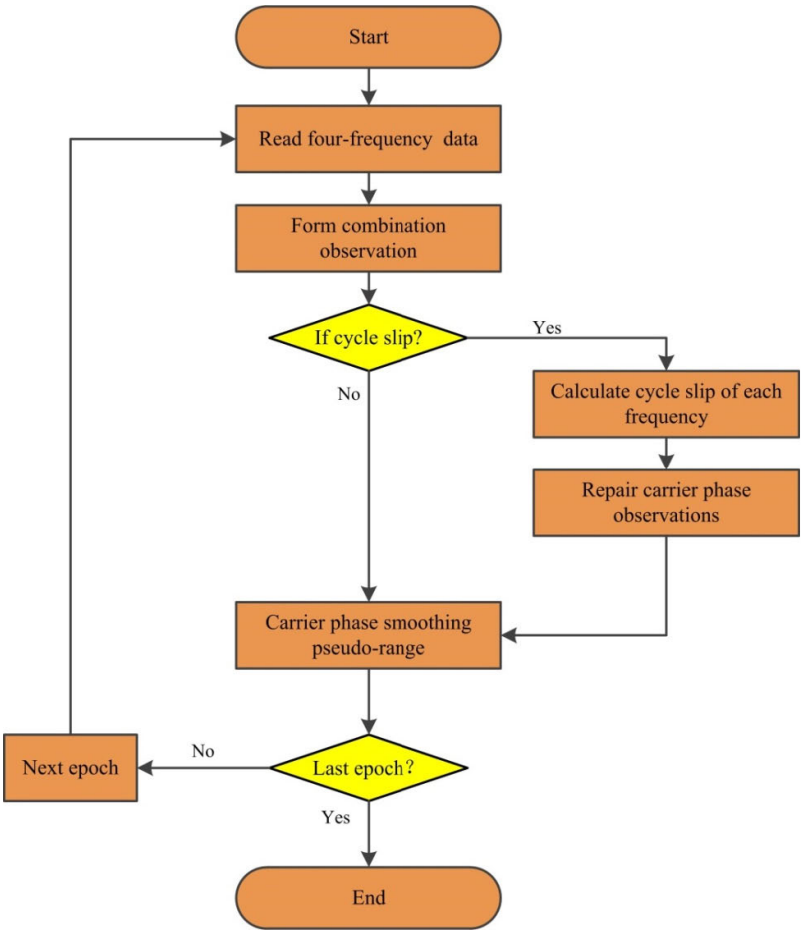

FIGURE 1. Galileo four-frequency CDR processing flow chart.

equation is presented as follows:

$$\begin{cases} \hat{\rho}_1^n = \dfrac{n-1}{n}[\hat{\rho}_1^{n-1} + \Delta\Phi_1^n + \dfrac{2}{1-r_{12}}\Delta(d\Phi_{12}^n)] + \dfrac{1}{n}\rho_1^n \\ \hat{\rho}_2^n = \dfrac{n-1}{n}[\hat{\rho}_2^{n-1} + \Delta\Phi_2^n + \dfrac{2r_{12}}{1-r_{12}}\Delta(d\Phi_{12}^n)] + \dfrac{1}{n}\rho_2^n \\ \hat{\rho}_3^n = \dfrac{n-1}{n}[\hat{\rho}_3^{n-1} + \Delta\Phi_3^n + \dfrac{2}{1-r_{13}}\Delta(d\Phi_{13}^n)] + \dfrac{1}{n}\rho_3^n \\ \hat{\rho}_4^n = \dfrac{n-1}{n}[\hat{\rho}_4^{n-1} + \Delta\Phi_4^n + \dfrac{2r_{13}}{1-r_{13}}\Delta(d\Phi_{13}^n)] + \dfrac{1}{n}\rho_4^n \end{cases} \tag{25}$$

with,

$$\begin{cases} r_{12} = (\dfrac{f_1}{f_2})^2;\ r_{13} = (\dfrac{f_1}{f_3})^2 \\ \Delta\Phi_m^n = \lambda_m(\varphi_m^n - \varphi_m^{n-1}) \end{cases} \tag{26}$$

$$\begin{cases} d\Phi_{12}^n = \Phi_2^n - \Phi_1^n;\ \Delta(d\Phi_{12}^n) = d\Phi_{12}^n - d\Phi_{12}^{n-1} \\ d\Phi_{13}^n = \Phi_3^n - \Phi_1^n;\ \Delta(d\Phi_{13}^n) = d\Phi_{13}^n - d\Phi_{13}^{n-1} \\ d\Phi_{14}^n = \Phi_4^n - \Phi_1^n;\ \Delta(d\Phi_{14}^n) = d\Phi_{14}^n - d\Phi_{14}^{n-1} \end{cases} \tag{27}$$

where n denotes the epoch number. ρ_m^n refers to the pseudo-range of the frequency $m = 1, 2, 3, 4$. $\hat{\rho}_m^n$ represents the pseudo-range after smoothing. In brief, the Galileo four-frequency CDR data processing flow can be obtained, as illustrated in Figure 1.

IV. DATA TEST AND ANALYSIS

A. EXPERIMENT ONE

In terms of the experimental data, Galileo four-frequency observation from station CUT0 in Curtin University, Australia was employed. The data were acquired in December 16, 2018 (DOY 350, 2018). The sampling interval was 30 s. The observations of E1, E5a, E5b, and E5 of the E12 satellite was delved into, respectively. To select the best detection quantity, two schemes were adopted:

Scheme 1: Four pseudo-range and carrier phase combinations: (−3, 1, −1, 4), (0, −1, 1, 0), (0, −1, 2, −1) and (1, −1, 0, 0).

Scheme 2: Three geometry-free carrier phase combinations (0, 1, 0, −1), (1, 1, −1, −1), (1, 2, −2, −1) and a geometry-free and ionosphere-free combination (0, 0, 1, −1).

Given that there was no cycle slip in the raw observation, the cycle slips were manually added to the raw carrier phase observation. The size and position of the cycle slip are listed in Table 7 and Table 8, respectively. Figure 2 to

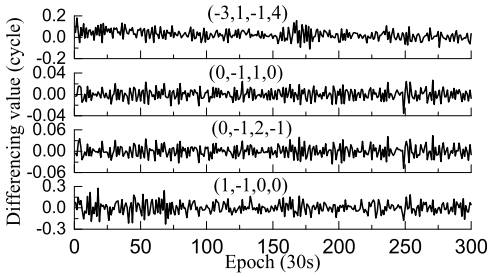

(a) (E1: 0 cycle, E5a: 0 cycle, E5b: 0 cycle, E5:0 cycle)

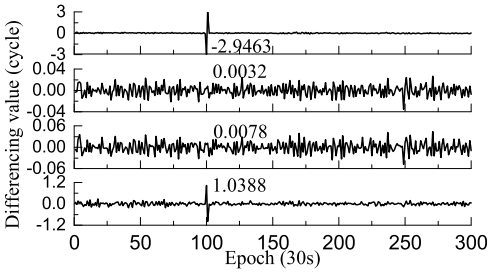

(b) (E1:1 cycle, E5a: 0 cycle, E5b: 0 cycle, E5: 0 cycle)

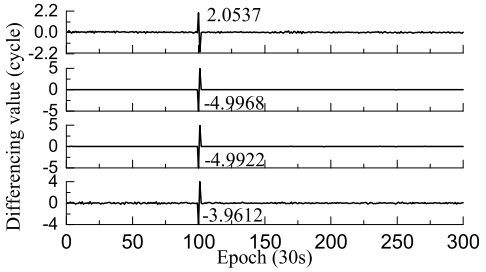

(c) (E1:1 cycle, E5a: 5cycle, E5b:0 cycle, E5:0 cycle)

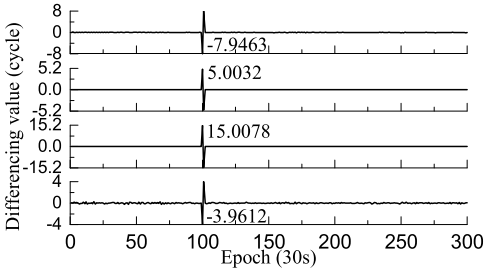

(d) (E1:1 cycle, E5a: 5 cycle, E5b: 10 cycle, E5: 0 cycle)

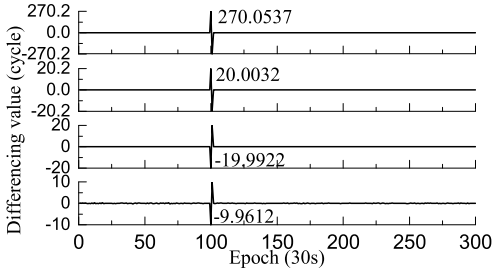

(e) (E1:10 cycle, E5a: 20 cycle, E5b: 40 cycle, E5: 80 cycle)

FIGURE 2. The differencing value of cycle slip detection combination for scheme 1 at E12 satellite.

Figure 3 present the time series of the cycle slip detection of E12 satellites under the two schemes, respectively.

The amplitudes of the pseudo-range and carrier phase combinations (−3, 1,−1, 4), (0, −1, 1, 0), (0, −1, 2, −1) and (1, −1, 0, 0) are nearly [−0.2, 0.2] cycle, [−0.04, 0.04] cycle, [−0.06, 0.06] and [−0.3, 0.3] cycle, respectively, as presented in Figure 2 (a). The amplitude of the geometry-free carrier phase combinations (0, 1, 0, −1), (1, 1, −1, −1) (1, 2, −2, −1) and the geometry-free and ionosphere-free combination (0, 0, 1, −1) are nearly [−0.01, 0.01] cycle, [−0.01, 0.01] cycle, [−0.01, 0.01] cycle and [−0.02, 0.02] cycle, respectively, as given in Figure 3 (a). Figure 2 (b-e) and Table 7 suggest that the deviations between the differencing and the theoretical values of four detection combinations are 0.0537 cycle, 0.0032 cycle, 0.0078 cycle and 0.0388 cycle, respectively. As showed in Figure 3 (b-e), and Table 8, the deviations between the differencing and the theoretical values of four detection combinations are 0.0010 cycle, 0.0028 cycle, 0.0025 cycle and 0.0022 cycle, respectively. In summary, the cycle slip detection capability of Galileo four-frequency geometry-free carrier phase combination is better than the pseudo-range and carrier phase combination.

To further verify the feasibility of the cycle slip detection after the Galileo pseudo-range observations were smoothed, the small cycle slips from (0, 0, 0, 1) to (3, 3, 3, 4) and the big cycle slips from (76, 76, 76, 77) to (79, 79, 79, 80) with an interval of 3 epochs were added in turn to the carrier phase observation. The E12 satellite in the detection results of small cycle slip and big cycle slip is presented in Figure 4 and Figure 5, respectively.

Figure 4 and Figure 5 reveal that all cycle slips were correctly detected by the geometry-free carrier phase combinations (0, 1, 0, −1), (1, 1, −1, −1), (1, 2, −2, −1) and a geometry-free and ionosphere-free combination (0, 0, 1, −1), and other satellites achieved similar results. Table 9 summarizes the success rate of cycle slip repair between original observation and CPSP, respectively. Table 9 indicates that the minimum success rate of the cycle slip repair calculated using the rounding method was 75.00% before smoothing. After the CPSP processing, the minimum success rate of the cycle slip

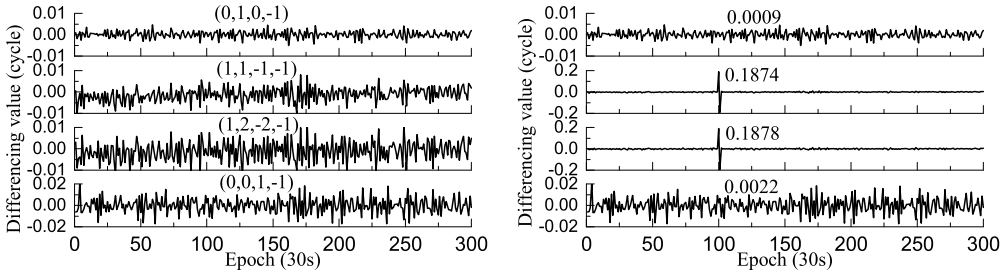

(a) (E1:0 cycle, E5a: 0 cycle, E5b: 0 cycle, E5: 0 cycle) (b) (E1:1 cycle, E5a: 0 cycle, E5b: 0 cycle, E5: 0 cycle)

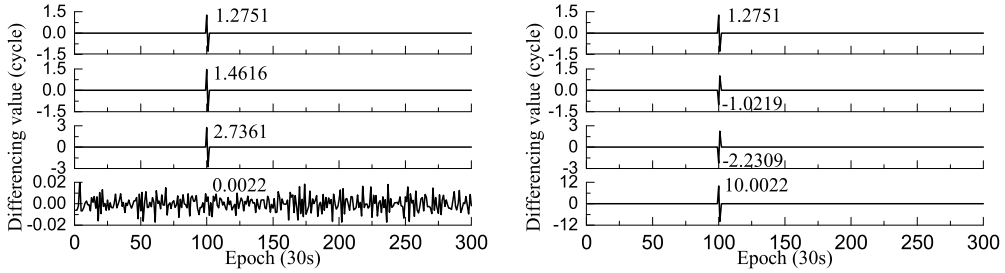

(c) (E1:1 cycle, E5a: 5 cycle, E5b: 0 cycle, E5:0 cycle) (d) (E1:1 cycle, E5a: 5 cycle, E5b: 10 cycle, E5: 0 cycle)

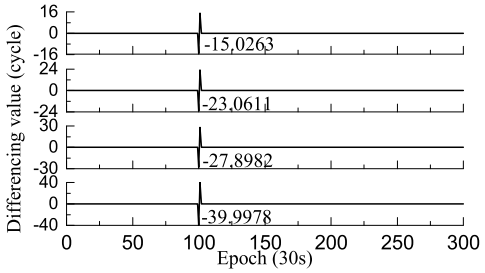

(e) (E1: 10 cycle, E5a: 20 cycle, E5b: 40 cycle, E5: 80 cycle)

FIGURE 3. **The differencing value of cycle slip detection combination for scheme 2 at E12 satellite.**

TABLE 7. **The location of added cycle slip combinations and cycle slip detection values in scheme 1.**

The location of cycle slip/epoch	Cycle slips	Cycle slip detection theoretical values			
		(-3, 1, -1, 4)	(0, -1, 1, 0)	(0, -1, 2, -1)	(1, -1, 0, 0)
100	(1, 0, 0, 0)	-3	0	0	1
	(1, 5, 0, 0)	2	-5	-5	-4
	(1, 5, 10, 0)	-8	5	15	-4
	(10, 20, 40, 80)	270	20	-20	-10

repair reached 99.99%. The difference between the floating value and the true cycle slip value is greatly reduced after smoothing. The smaller the influence of the pseudo-range noise, the higher the success rate of the cycle slip repair.

Figure 6 to Figure 7 illustrate the difference between the floating and true values of the cycle slip before and after the pseudo range smoothing of E04, E18, E21, and E30 satellites, respectively. The root mean square (RMS) value between floating and true values of each frequency before and after CPSP is listed in Table 10. Figure 6 to Figure 7 suggest that before smoothing, some deviations were greater than 0.5 cycle, revealing that it is not a feasible method to directly obtain the cycle slip by rounding. After the CPSP processing was performed, the deviation between the floating value and the true value was significantly less than 0.5 cycle, suggesting that the cycle slip can be correctly obtained by rounding. It can be seen from Table 10 that the differences of the RMS between float and true values were down-regulated by 79.61%, 70.03%, 66.25% and 72.75% after smoothing, respectively. In summary, the Galileo four-frequency CDR was effectively performed by the proposed method.

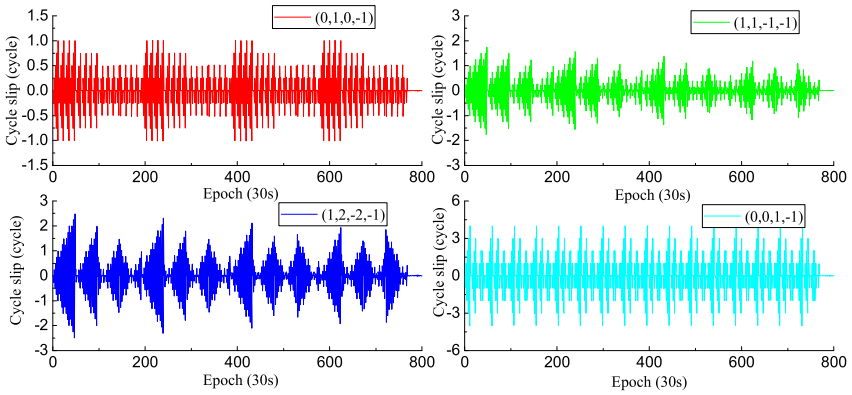

FIGURE 4. Time series of the small cycle slip detections with E12 satellite.

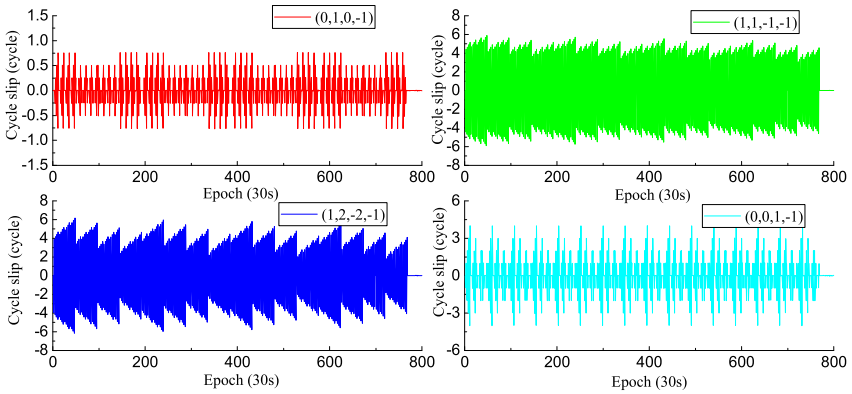

FIGURE 5. Time series of the big cycle slip detections with E12 satellite.

TABLE 8. The location of add cycle slip combinations and cycle slip detection values in scheme 2.

The location of cycle slip/epoch	Cycle slips	Cycle slip detection theoretical values			
		(0, 1, 0, -1)	(1, 1, -1, -1)	(1, 2, -2, -1)	(0, 0, 1, -1)
100	(1, 0, 0, 0)	0	0.1903	0.1903	0
	(1, 5, 0, 0)	1.2741	1.4644	2.7386	0
	(1, 5, 10, 0)	1.2741	-1.0191	-2.2284	10
	(10, 20, 40, 80)	-15.0272	-23.0582	-27.8957	-40.000

TABLE 9. The success rate of cycle slips repair between original observation and CPSP (%).

	Satellite								
	E04	E12	E13	E18	E19	E21	E24	E30	E31
Original	92.58	88.67	82.03	98.05	75.00	91.02	92.58	88.28	86.72
Smoothed	100.00	100.00	100.00	100.00	100.00	100.00	99.22	100.00	99.70

B. EXPERIMENT TWO

To verify the applicability of the proposed algorithm in active ionospheric area, the time series of the Dst (Disturbance Storm Time) index for 30 consecutive days in August 2018 are presented in Figure 8. This figure shows that the intense geomagnetic storm occurred on August 26 (the Dst index is less than −100nt). The peak value of Dst index was −174 nt. Figure 9 gives the global TEC (Total Electron Content) change chart at 6:00 on August 26. Fig. 9 suggests that the TEC varied significantly at 15° N and 125° E. Accordingly, a PTAG station was adopted to verify the feasibility of the proposed algorithm.

TABLE 10. The RMS value between floating value and the true value of each frequency before and after CPSP (cycle).

Satellite	Original				Smoothed			
	E1	E5a	E5b	E5	E1	E5a	E5b	E5
E04	0.325	0.245	0.251	0.249	0.053	0.052	0.053	0.052
E12	0.568	0.409	0.015	0.268	0.067	0.076	0.066	0.065
E13	0.611	0.463	0.473	0.469	0.102	0.121	0.112	0.101
E18	0.220	0.165	0.168	0.167	0.035	0.044	0.035	0.034
E19	0.752	0.568	0.582	0.574	0.095	0.104	0.096	0.093
E21	0.316	0.241	0.246	0.244	0.082	0.100	0.091	0.080
E24	0.492	0.384	0.392	0.388	0.152	0.162	0.153	0.162
E30	0.332	0.255	0.261	0.258	0.086	0.095	0.099	0.085
E31	0.622	0.486	0.495	0.491	0.191	0.210	0.181	0.180
Average value	0.471	0.357	0.320	0.345	0.096	0.107	0.108	0.094

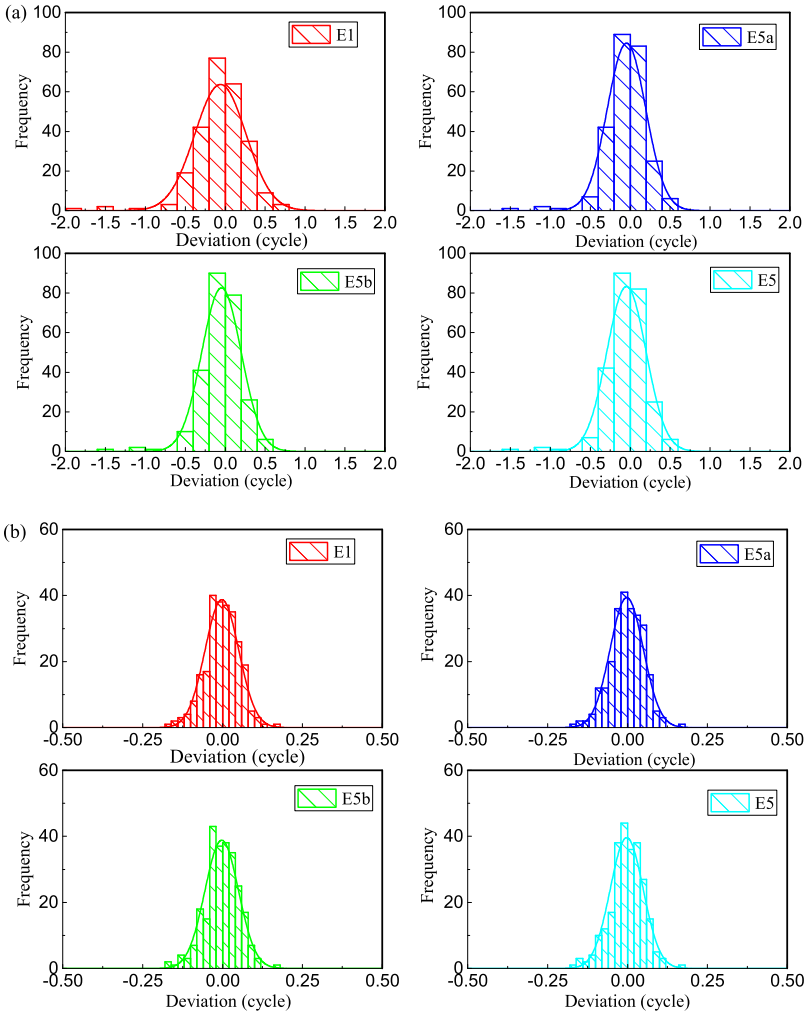

FIGURE 6. The difference between the floating value and true value of each frequency of E04 satellite (a: Original, b: Smoothed).

Since there was no cycle slip in the raw observation, the cycle slips were manually added to the raw carrier phase observation. The size and position of the cycle slip are listed in Table 11. Figure 10 presents the time series of the cycle slip detection of E02 satellite. The amplitude of the geometry-free carrier phase combinations (0, 1, 0, −1), (1, 1, −1, −1)

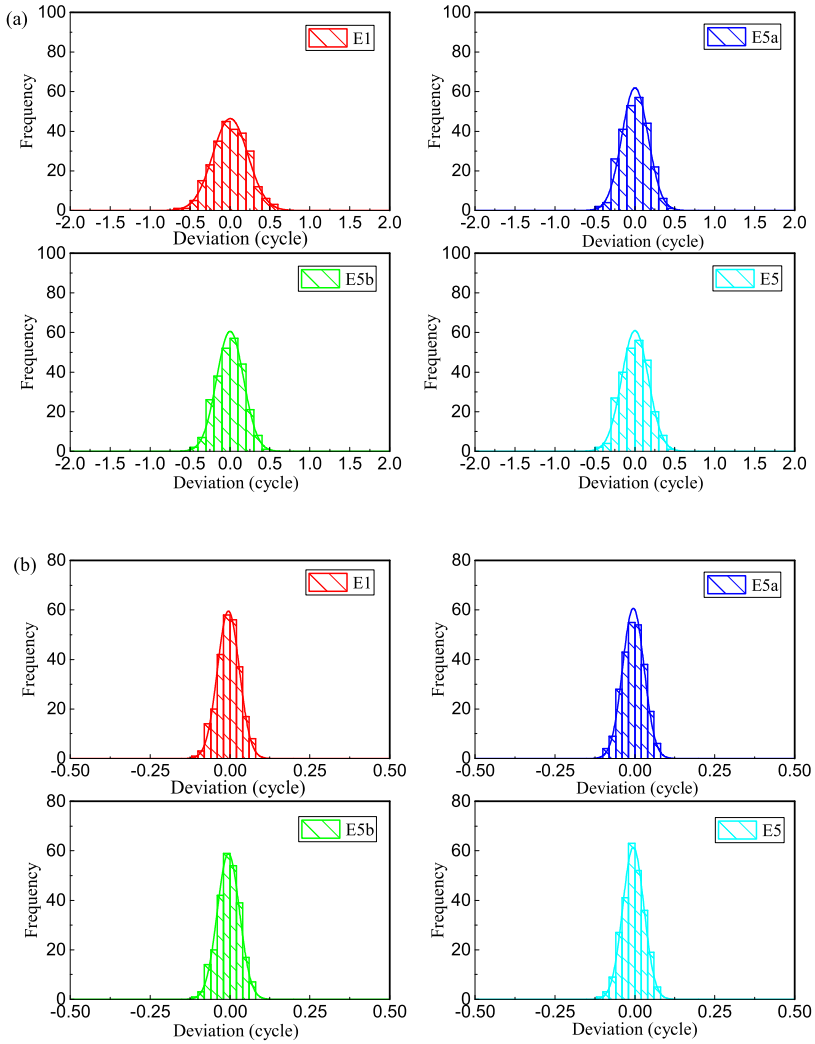

FIGURE 7. The difference between the floating value and true value of each frequency of E18 satellite (a: Original, b: Smoothed).

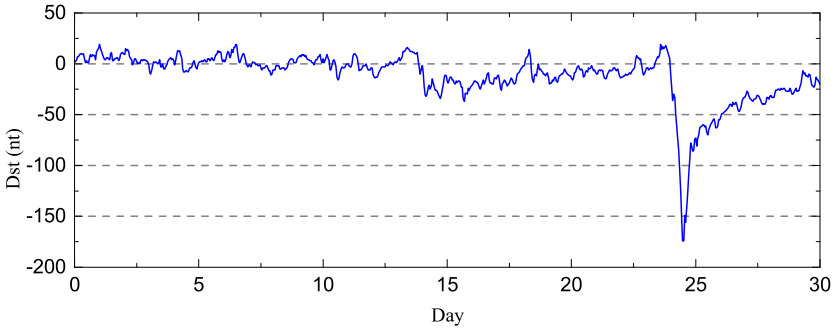

FIGURE 8. The time series of the Dst index for 30 consecutive days in August 2018.

(1, 2, −2, −1) and the geometry-free and ionosphere-free combination (0, 0, 1, −1) were nearly [−0.01, 0.01] cycle, [−0.03, 0.03] cycle, [−0.03, 0.03] cycle and [−0.02, 0.02] cycle, respectively, as presented in Figure 10 (a). According to Figure 10 (b-e), and Table 11, the deviations between the differencing and the theoretical values of four detection combinations were 0.0006 cycle, 0.0114 cycle, 0.0101 cycle and 0.0003 cycle, respectively.

To further verify the feasibility of the cycle slip detection after the Galileo pseudo-range observations were smoothed, the cycle slips from (76, 76, 76, 77) to (79, 79, 79, 80) with an interval of 3 epochs were added in sequence for carrier phase observation. Table 9 lists the success rate of cycle slip repair between original observation and CPSP, respectively, indicating that the minimum success rate of the cycle slip repair calculated with the rounding method

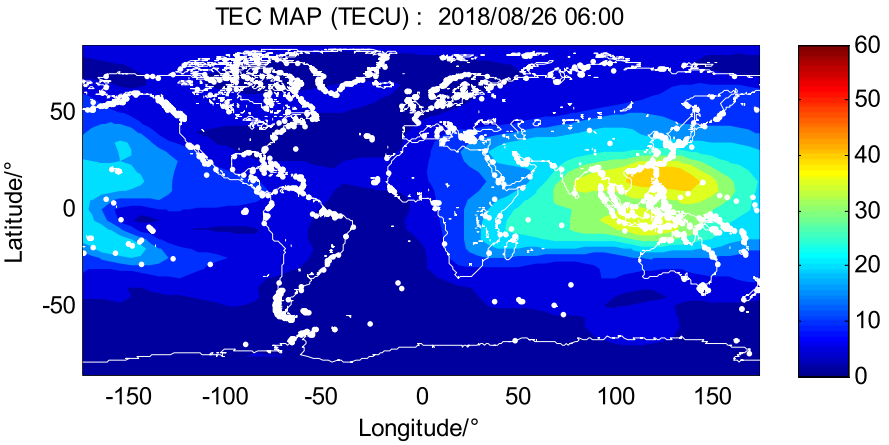

FIGURE 9. The global TEC change chart at 6:00 on August 26.

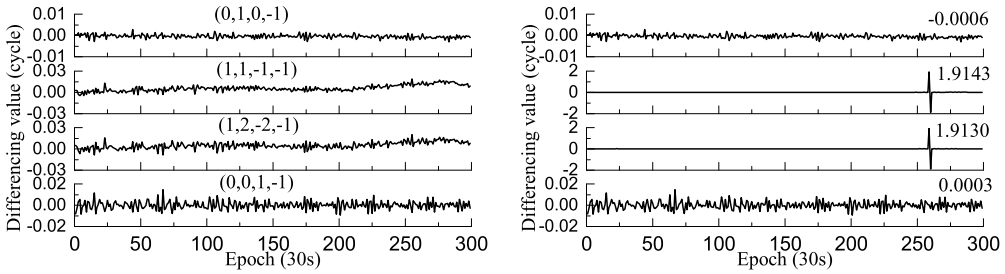

(a) (E1: 0 cycle, E5a: 0 cycle, E5b: 0 cycle, E5:0 cycle) (b) (E1:10 cycle, E5a: 0 cycle, E5b: 0 cycle, E5: 0 cycle)

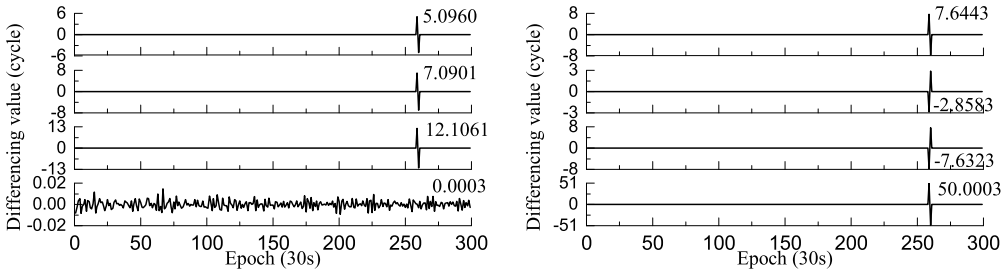

(c) (E1:10 cycle, E5a: 20 cycle, E5b:0 cycle, E5:0 cycle) (d) (E1:10 cycle, E5a: 30 cycle, E5b: 50 cycle, E5: 0 cycle)

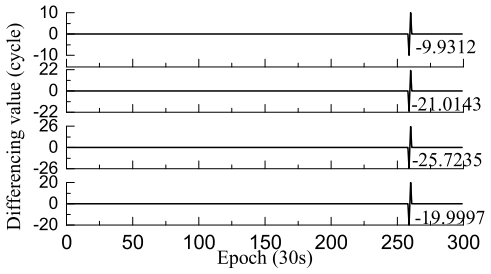

(e) (E1:20 cycle, E5a: 40 cycle, E5b: 60 cycle, E5: 80 cycle)

FIGURE 10. The differencing value of cycle slip detection combination for E02 satellite.

was 83.20% before smoothing. After the CPSP processing, the minimum success rate of the cycle slip repair reached 99.05%. The difference between the floating value and the true cycle slip value was considerably reduced after smoothing. Table 10 lists the RMS value between floating and true values of each frequency before and after CPSP, suggesting

TABLE 11. The location of add cycle slip combinations and cycle slip detection values.

The location of cycle slip/epoch	Cycle slips	Cycle slip detection theoretical values			
		(0, 1, 0, -1)	(1, 1, -1, -1)	(1, 2, -2, -1)	(0, 0, 1, -1)
260	(10, 0, 0, 0)	0	1.9029	1.9029	0
	(10, 20, 0, 0)	5.0966	6.9995	12.0961	0
	(10, 30, 50, 0)	7.6448	-2.8697	-7.6423	50
	(20, 40, 60, 80)	-9.9306	-21.0257	-25.7336	-20.000

TABLE 12. The success rate of cycle slips repair between original observation and CPSP (%).

	Satellite					
	E02	E03	E08	E19	E26	E27
Original	88.28	96.48	94.53	94.92	98.53	83.20
Smoothed	99.36	99.05	99.05	99.83	100.00	99.28

TABLE 13. The RMS value between floating value and the true value of each frequency before and after CPSP (cycle).

Satellite	Original				Smoothed			
	E1	E5a	E5b	E5	E1	E5a	E5b	E5
E02	0.316	0.304	0.304	0.304	0.278	0.276	0.276	0.276
E03	0.203	0.195	0.194	0.194	0.173	0.172	0.171	0.171
E08	0.236	0.227	0.226	0.226	0.197	0.198	0.197	0.197
E19	0.171	0.163	0.160	0.160	0.136	0.137	0.136	0.135
E26	0.110	0.103	0.104	0.104	0.089	0.088	0.089	0.089
E27	0.373	0.360	0.361	0.361	0.342	0.337	0.337	0.338
Average value	0.235	0.225	0.225	0.225	0.203	0.201	0.201	0.201

TABLE 14. The location of add cycle slip combinations and cycle slip detection values.

The location of cycle slip/epoch	Cycle slips	Cycle slip detection theoretical values		
		(1, 1, -2)	(1, -2, 1)	(1, 3, -4)
200	(10, 0, 0)	1.9029	1.9029	10
	(10, 20, 0)	6.9995	-8.2902	70
	(30, 50, 70)	-16.3187	-2.3895	-100

that the differences of the RMS between float and true values were down-regulated by 13.62%, 10.67%, 10.67% and 10.67% after smoothing, respectively. In brief, the Galileo four-frequency CDR was effectively performed using the proposed method in an active ionospheric area.

C. EXPERIMENT THREE

To verify the applicability of the proposed algorithm to triple-frequency cycle slip detection and repair, the test data originated from CUT0 station, and the data time was December 16, 2018. The observations were adopted through E1, E5a, and E5b observations of Galileo E01 satellite.

Since there was no cycle slip in the raw observation, the cycle slips were manually introduced to the raw carrier phase observation. The size and position of the cycle slip are listed in Table 14. Fig. 11 presents the time series of the cycle slip detection of E01 satellite. The amplitude of the geometry-free carrier phase combinations (1, 1, −2), (1, −2, 1) and the pseudo-range and carrier phase combination (1, 3, −4)

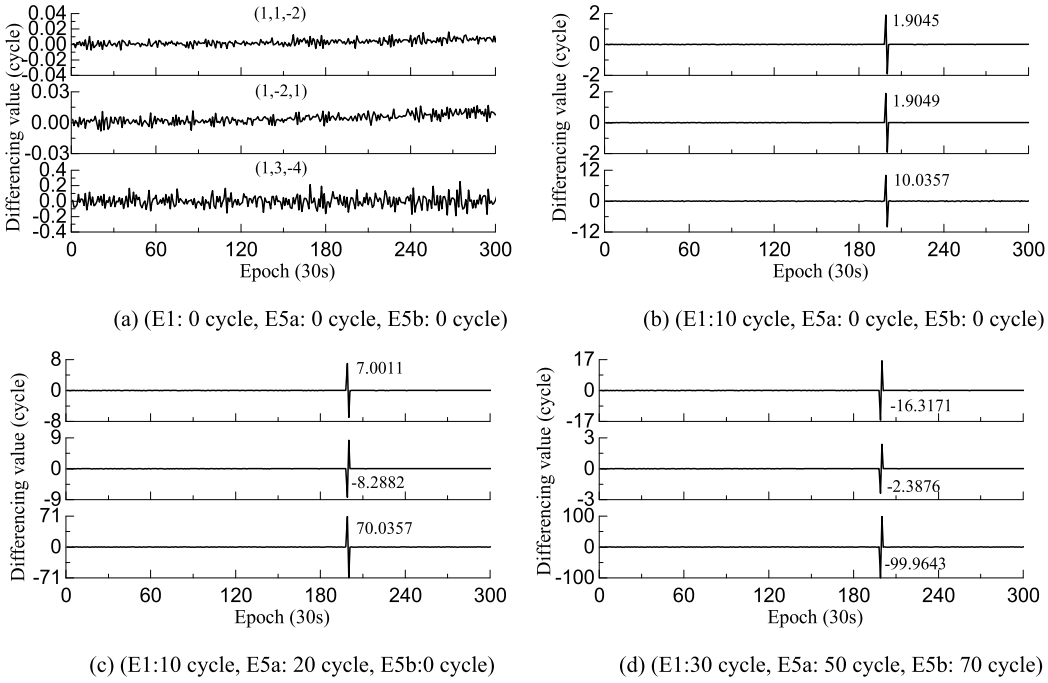

(a) (E1: 0 cycle, E5a: 0 cycle, E5b: 0 cycle)

(b) (E1:10 cycle, E5a: 0 cycle, E5b: 0 cycle)

(c) (E1:10 cycle, E5a: 20 cycle, E5b:0 cycle)

(d) (E1:30 cycle, E5a: 50 cycle, E5b: 70 cycle)

FIGURE 11. The differencing value of cycle slip detection combination for E01 satellite.

TABLE 15. The success rate of cycle slips repair between original observation and CPSP (%).

	Satellite					
	E02	E03	E08	E09	E14	E12
Original	81.28	73.61	76.85	72.52	81.11	70.83
Smoothed	99.54	99.55	100.00	100.00	100.00	100.00

TABLE 16. The RMS value between floating value and the true value of each frequency before and after CPSP (cycle).

Satellite	Original			Smoothed		
	E1	E5a	E5b	E1	E5a	E5b
E02	0.617	0.473	0.485	0.158	0.164	0.163
E03	0.425	0.329	0.336	0.138	0.142	0.141
E08	0.434	0.325	0.334	0.059	0.060	0.059
E09	0.580	0.441	0.451	0.102	0.103	0.105
E14	0.329	0.247	0.253	0.029	0.029	0.028
E12	0.514	0.385	0.394	0.054	0.054	0.055
Average value	0.483	0.367	0.376	0.090	0.092	0.092

were about [−0.02, 0.02] cycle, [−0.03, 0.03] cycle, and [−0.02, 0.02] cycle, respectively, as illustrated in Figure 11 (a). According to Figure 11 (b-d) and Table 11, the deviations between the differencing and the theoretical values of four detection combinations were 0.0016 cycle, 0.0020 cycle, and 0.0357 cycle, respectively.

To further verify the feasibility of the cycle slip detection after the Galileo pseudo-range observations were smoothed, the cycle slips from (76, 76, 76, 77) to (79, 79, 79, 80) with an interval of 3 epochs were added in sequence for carrier phase observation. Table 15 lists the success rate of cycle slip repair between original observation and CPSP, respectively, revealing that the minimum success rate of the cycle slip repair calculated with the rounding method was 70.83% before smoothing. After the CPSP processing, the minimum success rate of the cycle slip repair reached 99.54%. The difference between the floating value and the true cycle slip value was considerably reduced after smoothing. Table 16 lists the RMS

value between floating and true values of each frequency before and after CPSP, suggesting that the differences of the RMS between float and true values were down-regulated by 81.37%, 74.93% and 75.53% after smoothing, respectively. In brief, the Galileo triple-frequency CDR was effectively performed using the proposed method.

V. CONCLUSION

In this contribution, the features of Galileo four-frequency pseudo-range and carrier phase combination, geometry-free carrier phase combination and geometry-free and ionosphere-free combination were delved into. Given that the Galileo four-frequency CDR had been reported to be easily affected by the noise in pseudo-range observations, and a CPSP assisted CDR method was proposed. Such method exploits the non-divergent Hatch filter to perform the pseudo-range observation smoothly. To take the optimal combination of the CDR and verify the feasibility of the proposed method, the Galileo observations with different categories of satellites were performed and analyzed.

According to the experimental results, (1) The amplitude of the geometry-free carrier phase combinations (0, 1, 0, −1), (1, 1, −1, −1) (1, 2, −2, −1) is nearly [−0.01, 0.01] cycle, which are smaller than that of the pseudo-range and carrier phase combinations (−3, 1,−1, 4), (0, −1, 1, 0), (0, −1, 2, −1) and (1, −1, 0, 0). In summary, the cycle slip detection capability of Galileo four-frequency geometry-free carrier phase combination is better than the pseudo-range and carrier phase combination.

(2) Since the Galileo four-frequency geometry-free carrier phase combination is capable of forming up to three linear independent combinations, the geometry-free and ionosphere-free combination should be selected to build four linear independent combinations. In this contribution, the four linear independent combinations of the geometry-free carrier phase combination (0, 1, 0, −1), (1, 1, −1, −1), (1, 2, −2, −1) and geometry-free and ionosphere-free combination (0, 0, 1, −1) were employed for the detection of the cycle slip;

(3) The minimum success rate of the cycle slip repair with the original pseudo-range observation was 75.00%. After the CPSP processing, the minimum success rate of the cycle slip repair reached 99.99%. The difference between the floating value and the true cycle slip value is greatly reduced after smoothing. The smaller the influence of the pseudo-range noise, the higher the success rate of the cycle slip repair.

(4) The differences of the RMS between float and true values were down-regulated by 13.62%, 10.67%, 10.67% and 10.67% after smoothing, respectively. In summary, the Galileo four-frequency CDR was effectively performed by the proposed method in active ionospheric area. The differences of the RMS between float and true values were down-regulated by 81.37%, 74.93% and 75.53% after smoothing, respectively. In summary, the Galileo triple-frequency CDR was effectively performed by the proposed method.

ACKNOWLEDGMENT

The authors would like to thank the anonymous reviewers for their helpful suggestions.

REFERENCES

[1] S. Banville and R. B. Langley, "Mitigating the impact of ionospheric cycle slips in GNSS observations," *J. Geodesy*, vol. 87, no. 2, pp. 179–193, Feb. 2013.
[2] W. Gao, C. Gao, S. Pan, X. Meng, and Y. Xia, "Inter-system differencing between GPS and BDS for medium-baseline RTK positioning," *Remote Sens.*, vol. 9, no. 9, pp. 948–963, 2017.
[3] G. Xiao, M. Mayer, B. Heck, L. Sui, T. Zeng, and D. Zhao, "Improved time-differenced cycle slip detect and repair for GNSS undifferenced observations," *GPS Solutions*, vol. 22, no. 1, pp. 1–13, Jan. 2018.
[4] J. Chen, D. Yue, S. Zhu, H. Chen, Z. Liu, and X. Zhao, "Correction model of BDS satellite-induced code bias and its impact on precise point positioning," *Adv. Space Res.*, vol. 63, no. 7, pp. 2155–2163, Apr. 2019.
[5] H. Yuan, W. Wan, B. Ning, and J. Li, "A new cycle slip detection and correction method using triple differences solution," (in Chinese), *Acta Geodaetica Cartograph. Sinica*, vol. 27, no. 3, pp. 189–194, 1998.
[6] Y. G. Z. Li, "Cycle slip detection and ambiguity resolution algorithms for dual-frequency GPS data processing," *Mar. Geodesy*, vol. 22, no. 3, pp. 169–181, Jul. 1999.
[7] T. Yi, H. Li, and G. Wang, "Cycle slip detection and correction of GPS carrier phase based on wavelet transform and neural network," in *Proc. 6th Int. Conf. Intell. Syst. Design Appl.*, Oct. 2006, pp. 46–50.
[8] C. Wang and J. Wang, "Cycle slip detection and correction of single-frequency un-differenced phase observation," (in Chinese), *J. Tongji Univ. Natural Sci.*, vol. 40, no. 9, pp. 1393–1398, 2012.
[9] M. C. de Lacy, M. Reguzzoni, F. Sansò, and G. Venuti, "The Bayesian detection of discontinuities in a polynomial regression and its application to the cycle-slip problem," *J. Geodesy*, vol. 82, no. 9, pp. 527–542, Sep. 2008.
[10] F. Li, J. Gao, Z. Li, N. Qian, L. Yang, and Y. Yao, "A step cycle slip detection and repair method based on double-constraint of ephemeris and smoothed pseudorange," *Acta Geodyn. Geomater.*, vol. 16, no. 4, pp. 337–348, 2019.
[11] G. Blewitt, "An automatic editing algorithm for GPS data," *Geophys. Res. Lett.*, vol. 17, no. 3, pp. 199–202, Mar. 1990.
[12] L. Jing-Nan and G. Mao-Rong, "PANDA software and its preliminary result of positioning and orbit determination," *Wuhan Univ. J. Natural Sci.*, vol. 8, no. 2, pp. 603–609, 2004.
[13] M. Soycan, "A quality evaluation of precise point positioning within the Bernese GPS software version 5.0," *Arabian J. Sci. Eng.*, vol. 37, no. 1, pp. 147–162, 2012.
[14] N. Liu, Y. Xiong, and S. Xu, "Detection and repair of cycle slips using improved turboedit algorithm and Chebyshev polynomial method," (in Chinese), *Geomatics Inf. Sci. Wuhan Univ.*, vol. 36, no. 12, pp. 1500–1503, 2011.
[15] Z. Liu, "A new automated cycle slip detection and repair method for a single dual-frequency GPS receiver," *J. Geodesy*, vol. 85, no. 3, pp. 171–183, Mar. 2011.
[16] S. Ji, W. Chen, D. Weng, Z. Wang, and X. Ding, "A study on cycle slip detection and correction in case of ionospheric scintillation," *Adv. Space Res.*, vol. 51, no. 5, pp. 742–753, Mar. 2013.
[17] C. Cai, Z. Liu, P. Xia, and W. Dai, "Cycle slip detection and repair for undifferenced GPS observations under high ionospheric activity," *GPS Solutions*, vol. 17, no. 2, pp. 247–260, Apr. 2013.
[18] R. Duan, X. Zhao, C. Pang, and Y. Li, "Improved cycle slip detection and repair method for GPS receiver based on TurboEdit algorithm," (in Chinese), *Chin. J. Sci. Instrum.*, vol. 36, no. 11, pp. 2487–2494, 2015.
[19] T. Richert and N. El-Sheimy, "Optimal linear combinations of triple frequency carrier phase data from future global navigation satellite systems," *GPS Solutions*, vol. 11, no. 1, pp. 11–19, 2007.
[20] X. Li, G. Liu, X. Li, F. Zhou, G. Feng, Y. Yuan, and K. Zhang, "Galileo PPP rapid ambiguity resolution with five-frequency observations," *GPS Solutions*, vol. 24, no. 1, Jan. 2020.
[21] P. J. G. Teunissen and P. F. de Bakker, "Single-receiver single-channel multi-frequency GNSS integrity: Outliers, slips, and ionospheric disturbances," *J. Geodesy*, vol. 87, no. 2, pp. 161–177, Feb. 2013.

[22] G. Chang, T. Xu, Y. Yao, and Q. Wang, "Adaptive Kalman filter based on variance component estimation for the prediction of ionospheric delay in aiding the cycle slip repair of GNSS triple-frequency signals," *J. Geodesy*, vol. 92, no. 11, pp. 1241–1253, Nov. 2018, doi: 10.1007/s00190-018-1116-4.
[23] W. Liu, X. Jin, M. Wu, J. Hu, and Y. Wu, "A new real-time cycle slip detection and repair method under high ionospheric activity for a triple-frequency GPS/BDS receiver," *Sensors*, vol. 18, no. 2, pp. 427–448, 2018.
[24] B. Li, Y. Qin, and T. Liu, "Geometry-based cycle slip and data gap repair for multi-GNSS and multi-frequency observations," *J. Geodesy*, vol. 93, no. 3, pp. 399–417, Mar. 2019.
[25] Z. Dai, S. Knedlik, and O. Loffeld, "Real-time cycle-slip detection and determination for multiple frequency GNSS," in *Proc. 5th Workshop Positioning, Navigat. Commun.*, Hannover, Germany, Mar. 2008, pp. 37–43.
[26] L. Huang, L. Song, Y. Wang, and S. Zhi, "BeiDou triple-frequency geometry-free phase combination for cycle-slip detection and correction," (in Chinese), *Acta Geodaetica Cartogr. Sinica*, vol. 41, no. 5, pp. 763–768, 2012.
[27] Y.-F. Yao, J.-X. Gao, J. Wang, H. Hu, and Z.-K. Li, "Real-time cycle-slip detection and repair for BeiDou triple-frequency undifferenced observations," *Surv. Rev.*, vol. 48, no. 350, pp. 367–375, Sep. 2016.
[28] T. Zeng, L. Sui, Y. Xu, X. Jia, G. Xiao, Y. Tian, and Q. Zhang, "Real-time triple-frequency cycle slip detection and repair method under ionospheric disturbance validated with BDS data," *GPS Solutions*, vol. 22, no. 3, pp. 62–75, Jul. 2018.
[29] Q. Zhao, B. Sun, Z. Dai, Z. Hu, C. Shi, and J. Liu, "Real-time detection and repair of cycle slips in triple-frequency GNSS measurements," *GPS Solutions*, vol. 19, no. 3, pp. 381–391, Jul. 2015.
[30] X. Zhang and P. Li, "Benefits of the third frequency signal on cycle slip correction," *GPS Solutions*, vol. 20, no. 3, pp. 451–460, Jul. 2016.
[31] M. C. de Lacy, M. Reguzzoni, and F. Sansò, "Real-time cycle slip detection in triple-frequency GNSS," *GPS Solutions*, vol. 16, no. 3, pp. 353–362, Jul. 2012.
[32] B. Li, Y. Qin, Z. Li, and L. Lou, "Undifferenced cycle slip estimation of triple-frequency BeiDou signals with ionosphere prediction," *Mar. Geodesy*, vol. 39, no. 5, pp. 348–365, Sep. 2016.
[33] L. Huang, G. Zhai, Y. Ou, X. Lu, T. Wu, and K. Deng, "Triple-frequency TurboEdit cycle-slip processing method of weakening ionospheric activity," (in Chinese), *Acta Geodaetica Cartogr. Sinica*, vol. 44, no. 8, pp. 840–847, 2015.
[34] L. Van de Vyvere and R. Warnant, "Galileo cycle-slip detection," *GPS World*, vol. 27, no. 9, pp. 50–56, 2016.
[35] B. Park, K. Sohn, and C. Kee, "Optimal hatch filter with an adaptive smoothing window width," *J. Navigat.*, vol. 61, no. 3, pp. 435–454, Jul. 2008.
[36] L. Meng, J. Chen, J. Wang, and Y. Zhang, "CPSP aided real-time cycle slip detection and repair for triple-frequency un-differenced GNSS observation," (in Chinese), *J. Southeast Univ., Natural Sci. Ed.*, vol. 49, no. 3, pp. 573–580, 2019.

JIAN CHEN received the M.S. degree from the Anhui University of Science and Technology, in 2016. He is currently pursuing the Ph.D. degree with Hohai University. His research interests include GNSS precise positioning and RTK.

DONGJIE YUE received the Ph.D. degree in geodesy from Hohai University, Nanjing, Jiangsu, China. She is currently a Professor with the School of Earth Science and Engineering, Hohai University. Her main research activities include adjustment theory and high-precision GNSS positioning algorithms.

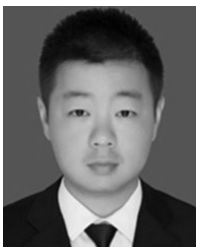

SHAOLIN ZHU received the M.S. degree from Hohai University, in 2018, where he is currently pursuing the Ph.D. degree. His research interests include GNSS precise positioning and RTK.

ZHIQIANG LIU received the Ph.D. degree in geodesy and surveying engineering from Tongji University, in 2015. He is currently an Assistant Professor with Hohai University. His current research interests include multi-GNSS PPP and real-time satellite clock estimation.

XINGWANG ZHAO received the Ph.D. degree from the School of Instrument Science and Engineering, Southeast University, Nanjing, China, in 2011. He is currently an Associate Professor with the School of Geodesy and Geomatics, Anhui University of Science and Technology, Huainan, China. His current research interest includes GNSS data processing.

WEI XU received the master's degree from the Anhui University of Science and Technology, in 2018. He is currently pursuing the Ph.D. degree with Wuhan University. His current research interests include multi-GNSS time transfer and its applications.